



High-frequency monitoring reveals how hydrochemistry and dissolved carbon respond to rainstorms at a karstic critical zone, Southwestern China

Caiqing Qin^a, Si-Liang Li^{a,b,c,*}, Susan Waldron^{d,a}, Fu-Jun Yue^{a,d}, Zhong-Jun Wang^b, Jun Zhong^a, Hu Ding^{b,d}, Cong-Qiang Liu^{a,b}

^a Institute of Surface-Earth System Science, Tianjin University, Tianjin 300072, China

^b State Key Laboratory of Environmental Geochemistry, Institute of Geochemistry, Chinese Academy of Sciences, Guiyang 550081, China

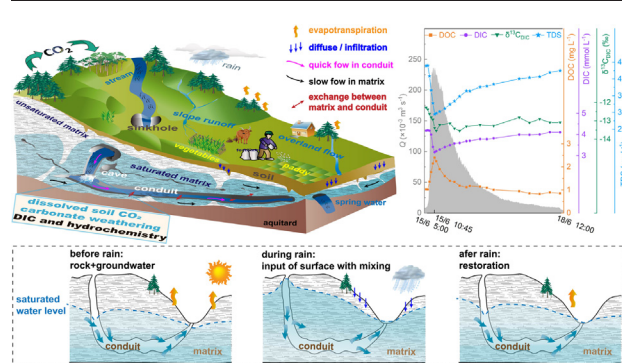
^c Puding Karst Ecosystem Observation and Research Station, Chinese Academy of Sciences, Puding 562100, China

^d School of Geographical and Earth Sciences, University of Glasgow, Glasgow G12 8QQ, United Kingdom

HIGHLIGHTS

- High-resolution data reveal the chemostatic behavior of HCO_3^- , Ca^{2+} and Mg^{2+} .
- NO_3^- and Cl^- are affected by throughflow flushing and show randomness behavior.
- Biologically-derived DIC controls DIC behavior during high discharge condition.
- DOC and DIC are regulated by transport-limited and process-limited, respectively.
- Hydrogeology, storm intensity and antecedent conditions affect solutes behavior.

GRAPHICAL ABSTRACT



ARTICLE INFO

Article history:

Received 18 September 2019

Received in revised form 19 January 2020

Accepted 19 January 2020

Available online 21 January 2020

Editor: José Virgílio Cruz

Keywords:

Water chemistry

Carbon dynamics

Chemical weathering

High-frequency monitoring

Chemostatic and hysteretic behavior

Karstic critical zone

ABSTRACT

Hydrochemical behavior and dissolved carbon dynamics are highly-sensitive to hydrological variations in the monsoon-influenced karstic critical zone which has high chemical weathering rates and experiences strong anthropogenic impact. Continuous high-frequency monitoring in the spring outlet of a karstic catchment in Southwestern China revealed that most hydrochemical variables changed distinctively in response to hydrologic variations, influenced by mixing of different sources and miscellaneous biogeochemical processes. Na^+ , K^+ and SO_4^{2-} varied significantly with hydrology, showing weak chemostatic behavior controlled by dilution. The flushing effect and random behavior of NO_3^- and Cl^- likely reflect agricultural inputs from high throughflow. Soil CO_2 in infiltrated water supports carbonate weathering, enabling DIC (dissolved inorganic carbon) and weathering products (e.g., Ca^{2+} and Mg^{2+}) to maintain chemostatic behavior. Biogenic DIC exhibited a stronger chemostatic response than carbonate sources and was the foremost control in DIC behavior. Carbon exchange between DIC and DOC (dissolved organic carbon) did not significantly influence DIC concentration and $\delta^{13}\text{C}$ due to very low DOC concentration. More DOC was exported by flushing from increasing discharge. Hysteretic analysis indicated that the transport processes were controlled by proximal sources mixing and diverse mobilization in various periods responding to rainstorms. NO_3^- and Cl^- presented different hysteresis behavior as sourced from agricultural activities. DOC increased on the hydrograph rising limb and was controlled by a transport-

* Corresponding author at: Institute of Surface-Earth System Science, Tianjin University, Tianjin 300072, China.

E-mail address: siliang.li@tju.edu.cn (S.-L. Li).

limited regime. However, the hysteresis behavior of most weathering products and DIC were regulated by a process-limited regime in the karstic critical zone. Overall, biogeochemical processes, hydrogeological properties, storm intensity/magnitude and the timing of storms (antecedent conditions) are main factors influencing the response of hydrochemical variables and dissolved carbon to storm events.

© 2020 Elsevier B.V. All rights reserved.

1. Introduction

The Earth's Critical Zone (CZ) is a heterogeneous environment containing air, water, soil, rock and living organisms. All these components interact, jointly regulating ecotopes (Brantley et al., 2006; Council, 2001). In the carbonate-dominated karstic critical zone (K-CZ), thin soil cover and well-developed conduit networks enable rapid transfer within the surface-underground systems, boosting fluid-rock interaction and intensifying hydrological influence in the CO₂-H₂O-CaCO₃ mixed system (Beaulieu et al., 2012; Yuan and Cai, 1988), where DIC concentration is about 66 times greater than in the CO₂-H₂O system (Dreybrodt, 1988). The world average flux of carbonate weathering and resultant consumption of atmospheric CO₂ are estimated to be about 1.29 Gt C yr⁻¹ and 0.15–1.6 Gt C yr⁻¹, respectively, both key terms in balancing carbon budgets despite uncertainty over the exact fluxes (Gaillardet et al., 1999; Martin, 2017). Fluid transport can affect hydrochemistry and carbon fate in the K-CZ (Khadka et al., 2014; Meybeck and Vörösmarty, 1999), and has global carbon flux of 0.8–1.2 Gt C yr⁻¹, with 38%, 25% and 37% respectively as DIC, DOC and particulate carbon (Amiotte-Suchet et al., 2003). Therefore, water is an essential mediator in the critical zone, and considering how hydrochemistry and dissolved carbon responds to changing hydrology offers insight to the crucial role of carbonate weathering, which influences the carbon cycle and ultimately climate change.

The monsoonal climate normally causes two contrasting seasons: a wet season with most annual precipitation, and a dry season with much less rain. In the wet season, storms and consequent runoff can alter hydrological conditions and dilute concentrations of solutes/nutrients, such as phosphorus and nitrate, in surface water (Bowes et al., 2015; Ferrant et al., 2013; Huang et al., 2018). This flow can transport solutes to, or accumulate in, the groundwater through eluviation, especially in agricultural karstic catchments where there are intensive farming activities and mature conduit systems (Buckerfield et al., 2019; Yue et al., 2019). The increasing discharge and solutes can accelerate carbonate weathering, offsetting dilution and enabling most weathering products to maintain chemostatic status (Clow and Mast, 2010; Musolff et al., 2015). On a catchment scale, relationships between concentrations (C) of dissolved solutes in fluid and flow discharge (Q) can in turn reflect chemostatic or chemodynamic export regimes (Musolff et al., 2015).

During one complete rainstorm, the C-Q relationships vary through time and generally exhibit loop trajectories when plotted due to hysteretic behavior (Williams, 1989). Williams (1989) categorized these hysteresis loops into five common hysteresis response classes, including single-valued line, clockwise loop, counterclockwise loop, single line plus loop, and figure-eight loop. Hysteresis analysis provides novel insight into the controls on catchment processes in response to rainstorms. It is useful for assessing the influence of storm behaviors on contributing sources of solutes and their flow pathways, and it has normally been used for explaining turbidity/sediment and some conventional nutrients (e.g., nitrate and phosphorus) (Baker and Showers, 2019; Bowes et al., 2005; Darwiche-Criado et al., 2015; Williams, 1989).

We have explored the controls on spatial-temporal variations in dissolved carbon and solutes on a seasonal or monthly basis in one K-CZ observatory in Southwestern China, the Houzhai catchment (Li et al., 2010; Qin et al., 2019; Yue et al., 2019). However, the existing researches lack the temporal resolution to detail the sensitivity of hydrochemistry and dissolved carbon dynamics to hydrological

variation. The recent advancements in in-situ sensors are increasing the availability of high-resolution discharge and hydrochemical data (Rode et al., 2016; van Geer et al., 2016; Yue et al., 2019). Coupled with high-frequency sampling, this paired approach can offer more detailed information on the response of biogeochemical processes to hydrological variation, for example to more accurately quantify carbonate weathering and carbon cycle in the K-CZ.

Thus, we adopted a combined sensor and field sampling programme in a sub-catchment of Houzhai catchment, the Chenqi catchment, to explore 1) the chemostatic response of hydrochemistry and dissolved carbon dynamics to rainstorms, 2) the hysteresis behavior of hydrochemistry and dissolved carbon under contrasting rainstorm conditions, and 3) the dominant controls on changes in hydrochemistry and dissolved carbon.

2. Materials and methods

2.1. Study area

The Chenqi catchment (26°15'20"–26°16'9"N, 105°46'3"–105°46'50"E), part of a K-CZ observatory, is a small (1.25 km²) agricultural karstic catchment (Fig. 1), within the Houzhai catchment (73.39 km²) which is central in the Southeast Asian Karst Region (the largest continuous karst area around the world) (Dianwu and Seip, 1991; Zhang et al., 2017). The Chenqi catchment is influenced by a subtropical monsoonal climate, 85.9% of annual rainfall (970 mm) occurred in the wet season in 2017, and the average air temperatures in the wet and dry season of 2017 were 21.3 °C and 11.2 °C, respectively.

The catchment altitude ranges from 1320 m (the outlet elevation) to 1520 m a.s.l. It is a peak-depression karstic landscape which is encircled by star-distributed conical hills. Carbonate rocks are widely distributed, and overlying Quaternary soils are erratically formed and irregularly spread (Chen et al., 2018). Limestone formations shape the higher elevation zones, with 150–200 m thickness above an impermeable marlite formation (Zhang et al., 2019). The soil on the hills is thin (mean < 50 cm), and hills are mainly covered with deciduous broad-leaved forest and scrub-grassland, occupying 83% of total land use. The soil on the lower part of gentle hillslopes and valley depressions is thicker (40–100 cm) and mostly used for farming land, accounting for ~17% area of this catchment (3% for paddy and 14% for dry land).

2.2. Sampling and measurement

High-frequency sampling campaigns were carried out at the spring outlet of Chenqi catchment (Fig. 1) from May 22nd to July 3rd and from August 12nd to August 15th in 2017. Triplicate samples were collected in clean and dry bottles, rinsed twice with spring water before sampling, and stored immediately in darkness at 4 °C prior for measuring alkalinity and the concentration of major ions and DOC, no later than 12 h after sampling. Water temperature (T), dissolved oxygen (DO), electrical conductivity (EC), pH, and discharge were continuously measured at high temporal resolution (15-minute interval) in the field using a multi-parameter probe (Aquatroll 600) and a flowmeter, calibrated approximately monthly.

Alkalinity was measured by acid titration with 0.02-M hydrochloric acid (HCl). Samples for the measurement of ion concentration were filtered through 0.22 μm cellulose-acetate filter paper and divided into two parts. One was acidified to pH = 2 by HNO₃ to measure major

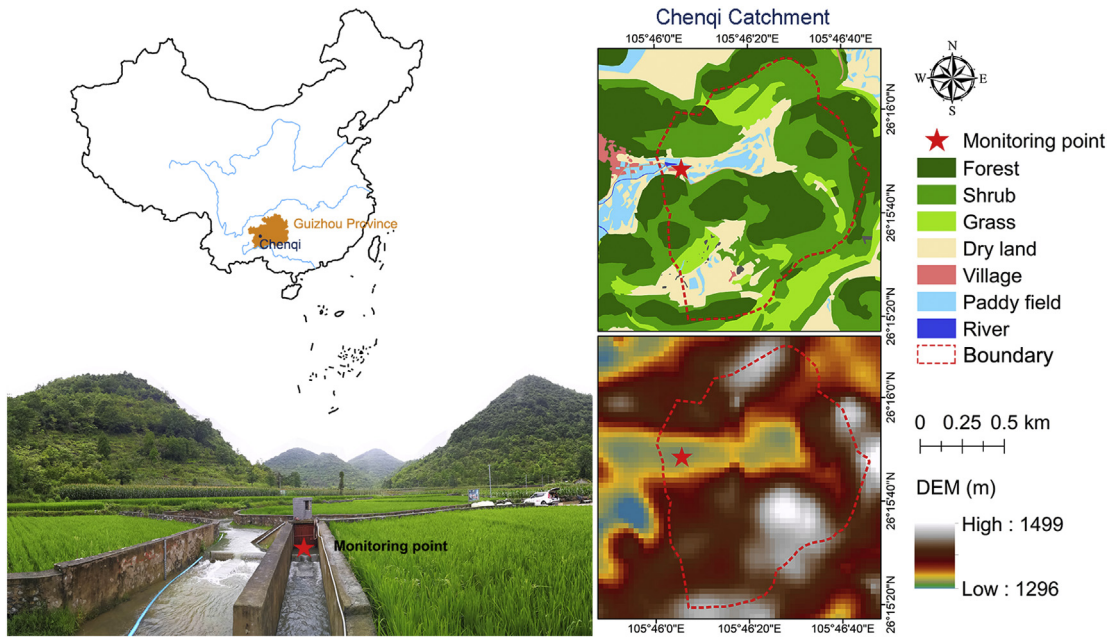


Fig. 1. Location of the study area and the land use patterns at Chenqi catchment.

cations (Ca^{2+} , Mg^{2+} , Na^+ , K^+) by inductively-coupled plasma optical emission spectrometer; the other unacidified filtrate was used for measuring main anions (SO_4^{2-} , Cl^- , NO_3^-) using ion chromatography. All measurements were within a relative standard deviation (RSD) of 5%. DOC concentration was measured using an OI Analytical Aurora 1030 TOC analyzer. To simplify the description, the square bracket “[]” was used as the notation for the concentration, e.g., [DOC] refers to DOC concentration.

Total dissolved solids (TDS) were calculated from the sum of above ions. Inorganic carbon species and the partial pressure of dissolved CO_2 ($p\text{CO}_2$) in water were calculated using methods similar to Qin et al. (2019). For the stable carbon isotopic composition of DIC ($\delta^{13}\text{C}_{\text{DIC}}$), a 15 mL water sample with no air bubbles was injected at the sampling site into an evacuated glass bottle containing 1 mL phosphoric acid (85%) and a magnetic stir bar (clean and dry) (adapted from Waldron et al. (2014)). The pretreatment of samples was conducted within one day after sampling. Briefly, the CO_2 was extracted on a vacuum line by stirring at a constant temperature of 50 °C and then purified cryogenically before storage in a glass vacuum tube for isotope analysis. $^{13}\text{C}/^{12}\text{C}$ (R) were measured by a Finnigan MAT 252 mass spectrometer with an accuracy of 0.2‰ and reported using the delta (δ) notation relative to the Vienna Pee Dee Belemnite (V-PDB) in per mil (‰) as follows:

$$\delta^{13}\text{C} (\text{‰}) = (R_{\text{sample}}/R_{\text{standard}} - 1) \times 10^3 \quad (1)$$

All containers were prewashed with hydrochloric acid and cleaned with Milli-Q water in the laboratory before use.

2.3. Data analysis

2.3.1. Chemostatic analysis

To analyze the sensitivity of solutes to discharge variation, a power-law function was fitted to the relationships between solute concentrations and discharge (Godsey et al., 2009) as follows:

$$C_i = a Q_i^b \quad (2)$$

where: C_i and Q_i are the instantaneous solute concentrations (C) at timestep i and the synchronous discharge (Q), respectively.

Exponent b is a useful index to mirror the chemostatic characteristics of solutes. If $b = -1$, the product of C and Q equals the constant solute flux of “ a ” and the dilution effect generated from increasing Q is the only control on C ; if $b = 0$, C equals the constant “ a ” and is independent of Q variation; if $-1 < b < 0$, the dilution effect and chemostatic behavior coexist; whereas if $b > 0$, there is enrichment with the inflow of high discharge.

2.3.2. Hysteresis analysis

To compare the hysteresis behavior of various parameters within or between different storms under diverse antecedent hydrological conditions, the hysteresis index (HI), a reasonable surrogate which can reflect the size and direction of hysteresis loop by dimensionless quantification, was calculated using normalised data (Lloyd et al., 2016b):

$$\text{Normalised } Q_i = (Q_i - Q_{\min}) / (Q_{\max} - Q_{\min}) \quad (3)$$

$$\text{Normalised } C_i = (C_i - C_{\min}) / (C_{\max} - C_{\min}) \quad (4)$$

$$\text{HI} = \text{Normalised } C_{i-RL} - \text{Normalised } C_{i-FL} \quad (5)$$

where: Q_i and C_i refer to the instantaneous discharge and concentrations at timestep i , Q_{\max}/Q_{\min} and C_{\max}/C_{\min} refer to the maximum/minimum value of discharge (Q) and concentration (C) during an individual complete event, respectively. Normalised C_{i-RL} and C_{i-FL} are the normalised measurements on the rising limb and on the corresponding falling limb at every 10% increment of the discharge hydrograph. 10% is an acceptable interval (Lloyd et al., 2016b). Therefore, every individual storm includes 9 HI values (from 10% to 90% of discharge, discarding the beginning and ending sections to eliminate interference). The distribution of the 9 HI values was used to analyze the hysteresis dynamics within the individual storm, and their mean was also calculated to represent the final HI value for each individual storm, allowing the comparison of different events.

According to the significance of HI defined above, HI should be between -1 and 1 , where the bigger the absolute value the wider the loop shape. Negative HI denote counterclockwise trajectories where concentrations of analytes are higher on the falling limb of discharge hydrograph, while positive values indicate clockwise loops where the concentrations are higher on the rising limb. Zero represents no

hysteretic effect or a symmetrical figure-eight pattern. HI values can also be used to deduce the length of the time lag between discharge peak and maximal concentrations of variables, the bigger the absolute values of HI the longer the lag (Lloyd et al., 2016b).

2.3.3. Evaluation of DIC sources

DIC sources can be identified using $\delta^{13}C_{DIC}$ (Clark and Fritz, 1997). DIC in natural groundwater is normally generated by carbonate weathering (carbonate source) and dissolution of soil CO₂ (biological source) which is mainly derived from root respiration and/or decomposition of labile soil organic matter in the soil zone (Li et al., 2010). In this region, $\delta^{13}C_{DIC}$ from carbonate and biological sources can be assumed as 0‰ and -18‰ respectively (Qin et al., 2019), and their contribution to DIC can be calculated by mass balance:

$$\delta^{13}C_{DIC} = \delta^{13}C_{bio} \times f_{(bio)} + \delta^{13}C_{carb} \times f_{(carb)} \tag{6}$$

$$DIC = DIC_{bio} + DIC_{carb} = DIC \times f_{(bio)} + DIC \times f_{(carb)} \tag{7}$$

where: $f_{(bio)}/DIC_{bio}$ and $f_{(carb)}/DIC_{carb}$ are the proportion/amount of DIC from the biological and carbonate sources, respectively.

This calculation is a simplified binary approach and so there is uncertainty from C cycling processes (e.g., equilibrium fractionation in water-air interface). However, it should work well for this research as sampling campaigns were conducted during high-flow periods when mixing and fast reaction are the dominant patterns under this nearly enclosed situation with high pCO₂ in spring water.

3. Results

3.1. Hydrologic and hydrochemical characteristics

Discharge at the spring outlet had an obvious seasonality during the hydrologic year of 2017, and ranged from 0.3×10^{-3} to $319.7 \times 10^{-3} \text{ m}^3 \text{ s}^{-1}$ during the sampling period (Fig. 2). All parameters responded to hydrological variation, although they also fluctuated in early June when there was no obvious discharge variation (Fig. 2). This is possibly due to the agricultural pumping and irrigation, which did not induce discharge variation but altered water hydrochemistry. Summary compositions of the manually-collected samples are showed

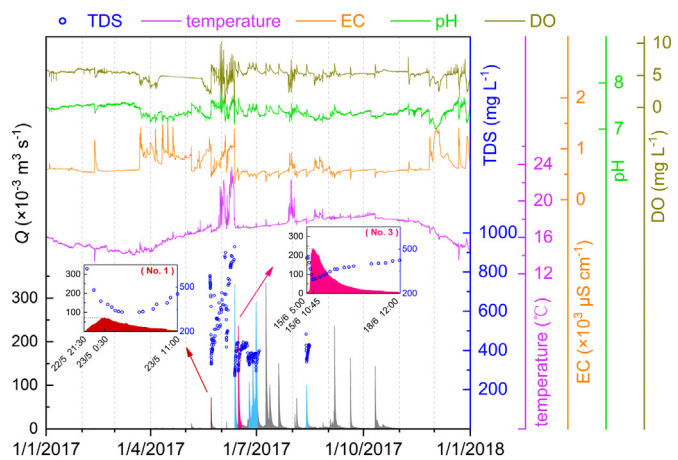


Fig. 2. Time series of discharge and water quality parameters throughout the whole year of 2017. And TDS (total dissolved solids) concentrations during sampling periods. In the time series graph of discharge, the gray area refers to periods without sampling campaigns but only high-resolution data from in-situ sensors; the claret and pink parts denote two representative individual rainstorms, namely storms No. 1 and No. 3 respectively (corresponding to two embedded small graphs), which are used as examples to expound hysteresis behavior; the sky-blue section includes other six individual rainstorms in Table 2. (For interpretation of the references to color in this figure legend, the reader is referred to the web version of this article.)

in Table 1. The spring water is mildly alkaline, with small pH fluctuation (7.2 to 7.7). The discharge-weighted mean concentrations (DWC) of cations follow the order of Ca²⁺ (1.64 mmol L⁻¹) > Mg²⁺ (0.42 mmol L⁻¹) > Na⁺ (0.05 mmol L⁻¹) > K⁺ (0.03 mmol L⁻¹), with the sum of Ca²⁺ and Mg²⁺ accounting for over 90%. For anion DWC, HCO₃⁻ (3.71 mmol L⁻¹) > SO₄²⁻ (0.38 mmol L⁻¹) > NO₃⁻ (0.24 mmol L⁻¹) > Cl⁻ (0.08 mmol L⁻¹), and HCO₃⁻ concentration is an order of magnitude higher than that of other anions. The dominance of Ca²⁺, Mg²⁺ and HCO₃⁻ is consistent with the characteristics of catchments draining carbonate-rich areas (de Montety et al., 2011; Perrin et al., 2008). TDS concentrations change with an opposite trend with discharge (Fig. 2), ranging from 270 to 930 mg L⁻¹. The DWC (340 mg L⁻¹) of TDS is more than three times the global DWC of 97 mg L⁻¹ (Li and Bush, 2015), and also higher than many basins draining karst terrain in China, e.g., the Beipanjiang River of 324 mg L⁻¹ (S.-L. Li et al., 2008), the Wujiang basin of 265 mg L⁻¹ (Zhong et al., 2017) and the Xijiang River of 160 mg L⁻¹ (Zhong et al., 2018), but lower than some northern rivers, e.g., the Liao River of 400 mg L⁻¹ (Ding et al., 2017) and the Huai River of 509 mg L⁻¹ (Zhang et al., 2011).

The total charge of dissolved cations and anions yields a highly significant correlation (R² = 0.97, n = 277) with the net inorganic charge balance (NICB) of within ±5%, and the calculated TDS also shows a significant positive correlation with the sensor-measured EC (R² = 0.98; n = 277). This suggests that other elements not measured make negligible contribution to dissolved solutes.

3.2. Dissolved carbon characteristics

In this study, [DIC] (=CO_{2(aq)} + H₂CO₃ + HCO₃⁻ + CO₃²⁻) and [DOC] ranged from 2.59 to 5.05 mmol L⁻¹ and from 0.63 to 3.24 mg L⁻¹, respectively (Table 1). However, their responses to discharge variation are different: higher discharge usually corresponds to higher [DOC] but lower [DIC] (Fig. 3). The DWC of DIC (3.71 mmol L⁻¹) is much higher than the world average level of 0.85 mmol L⁻¹ (Voss et al., 2014). The pCO₂ in spring water changed from 3.4×10^{-3} to 14.1×10^{-3} atm, which is far higher than that in atmosphere (0.4×10^{-3} atm). $\delta^{13}C_{DIC}$ ranged from -15.9‰ to -10.8‰, with a mean of -13.0‰. The variation in $\delta^{13}C_{DIC}$ with discharge is not significant, but lower $\delta^{13}C_{DIC}$ usually occurs at lower discharge (Fig. 3).

3.3. Chemostatic characteristics

Fig. 4 shows the ionic C-Q relationships defined using a power-law function. [Na⁺], [K⁺] and [SO₄²⁻] exhibit more negative b values, namely -0.248, -0.219 and -0.427, respectively, and their fitted curves are closer to rainwater dilution curves. Other ions have bigger b values, especially [HCO₃⁻] (-0.015) and [NO₃⁻] (-0.082), whose b values are close to 0. Of all ions, the power law describes the C-Q relationship of [HCO₃⁻] least well.

3.4. Hysteretic characteristics

A hydrological event here is defined as the response of discharge which begins with a rapid increase (>20% over baseflow) and ends when discharge returns to baseflow or increases again due to another event. Thus continual small storms, which induce discharge fluctuation only within $\pm 10 \times 10^{-3} \text{ m}^3 \text{ s}^{-1}$ or cannot be plotted as hysteresis loops due to short duration of clear rising or falling limb sections, are not taken into consideration. This approach generated eight hydrological events with different antecedent conditions for consideration (Table 2). Two hydrologically contrasting events (Fig. 2) were analyzed further: 'storm' No. 1 which occurred after a long period of relatively-dry conditions and continued for 13 h, and 'storm' No. 3 which lasted for 79 h and occurred immediately after another large event ('storm' No. 2).

Table 1

Statistical characteristics of hydrochemistry and dissolved carbon parameters during sampling period in this study.

	EC ($\mu\text{S cm}^{-1}$)	pH	Major ions (mmol L ⁻¹)								TDS (mg L ⁻¹)	DIC (mmol L ⁻¹)	DOC (mmol L ⁻¹)	pCO ₂ ($\times 10^{-3}$ atm)	$\delta^{13}\text{C}_{\text{DIC}}$ (‰)
			Ca ²⁺	Mg ²⁺ +	Na ⁺	K ⁺	HCO ₃ ⁻	SO ₄ ²⁻	NO ₃ ⁻	Cl ⁻					
Min	316	7.2	1.14	0.30	0.04	0.02	2.44	0.21	0.14	0.03	270	2.59	0.05	3.4	-15.9
Max	1148	7.7	4.67	1.70	0.23	0.12	4.60	4.24	0.58	0.28	930	5.05	0.27	14.1	-10.8
Mean	591	7.4	2.20	0.67	0.09	0.04	3.73	1.08	0.29	0.13	460	4.07	0.12	7.9	-13.0
DWC	449	/	1.64	0.42	0.05	0.03	3.71	0.38	0.24	0.08	340	3.71	0.13	/	/
S.D.	186.42	0.11	0.71	0.33	0.05	0.02	0.34	1.07	0.10	0.06	149	0.43	0.05	2.44	0.78
CV (%)	31.5	1.5	32.2	50.2	60.2	54.4	9.2	99.4	33.4	46.0	32.6	10.5	44.1	30.8	6.0

Note: S.D., DWC and CV refer to the standard deviation, discharge-weighted mean concentration ($\sum(Q_i \times C_i) / \sum Q_i$, C_i is the parameter concentration at timestep i and Q_i is the synchronous discharge) and coefficient of variation (the ratio of standard deviation to mean), respectively. The pH mean equals its median.

Ionic hysteresis behaviors differ between the two storms (Fig. 5), although all trajectories evidence dilution, plotting from the left upper corner to the right lower corner. During storm No.1 (Fig. 5(a)–(h)), hysteresis loops of most ions exhibit clockwise trajectories, but not NO₃⁻ and Cl⁻ whose behaviors tend to be figure-eight shapes. During storm No. 3 (Fig. 5(i)–(p)), clockwise loops of Ca²⁺, Mg²⁺, HCO₃⁻, SO₄²⁻ and Na⁺ are smaller in magnitude (HI values are near to 0) than that in storm No. 1, and tend towards counterclockwise. Conversely, hysteretic trajectories for K⁺, NO₃⁻ and Cl⁻ expand and show no obviously counterclockwise response, and have a similar distribution of 10%-discharge HI values (the embedded graphs in Fig. 5): bigger at high discharge and smaller at low discharge.

The hysteresis behaviors of normalised [DOC], [DIC] and $\delta^{13}\text{C}_{\text{DIC}}$ for storm No. 1 and No. 3 are shown in Fig. 6. [DOC] exhibits a figure-eight trajectory during storm No. 1 (Fig. 6(a)) but a full clockwise loop during storm No.3 (Fig. 6(d)), leading to an increase in HI values, from 0.12 ± 0.61 for storm No. 1 to 0.31 ± 0.06 for storm No. 3. [DOC] shows an ascending trend on the rising limb in both storms but increases more quickly than discharge during storm No. 1. Hysteresis trajectories of [DIC] and the distributions of 10%-discharge HI values are also different between the two storms, with bigger clockwise loops in

storm No. 1 (Fig. 6(b)) than in storm No. 3 (Fig. 6(e)). $\delta^{13}\text{C}_{\text{DIC}}$ does not show a simple hysteresis response, although its hysteresis loop tends to plot clockwise during both storms (Fig. 6(c) and (f)), with a mean HI value of 0.44 ± 0.24 for storm No. 1 and 0.33 ± 0.13 for storm No. 3.

4. Discussion

4.1. Controls on hydrochemical C-Q relationships

The negative relationships between ion concentrations and discharge (Fig. 4) caused by dilution occur as the dissolution kinetics and time available for mineral-water reactions are longer than the water residence time (Zhong et al., 2017). However, the data do not fit the rainwater dilution curves, indicating that there are some processes providing additional solute inputs with through-flow, counteracting the dilution effect and maintaining chemostatic (Clow and Mast, 2010).

The smaller b values of the fitted curves for [Na⁺], [K⁺] and [SO₄²⁻] (Fig. 4) indicate the slower release or lower quantities of these ions, such that the pool is more rapidly diluted by rainwater. However, the relatively strong chemostatic responses of [Ca²⁺], [Mg²⁺] and [HCO₃⁻] to increasing discharge are mostly likely due to carbonate weathering

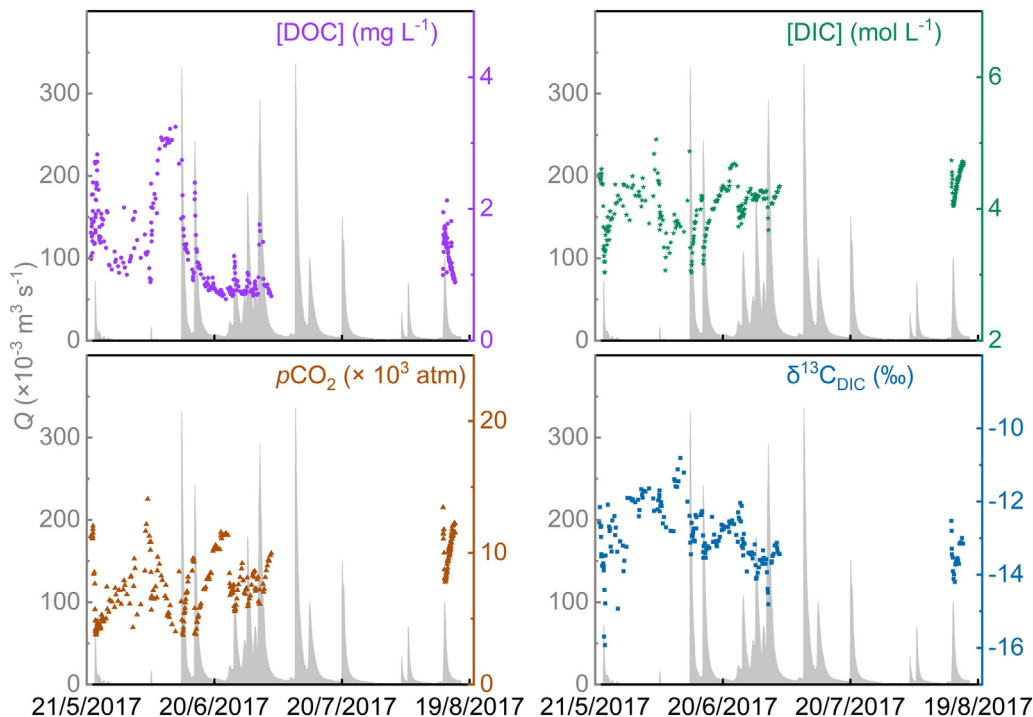


Fig. 3. Time series of DOC, DIC, pCO₂ and $\delta^{13}\text{C}_{\text{DIC}}$ during the sampling period, accompanying with real-time discharge (Q).

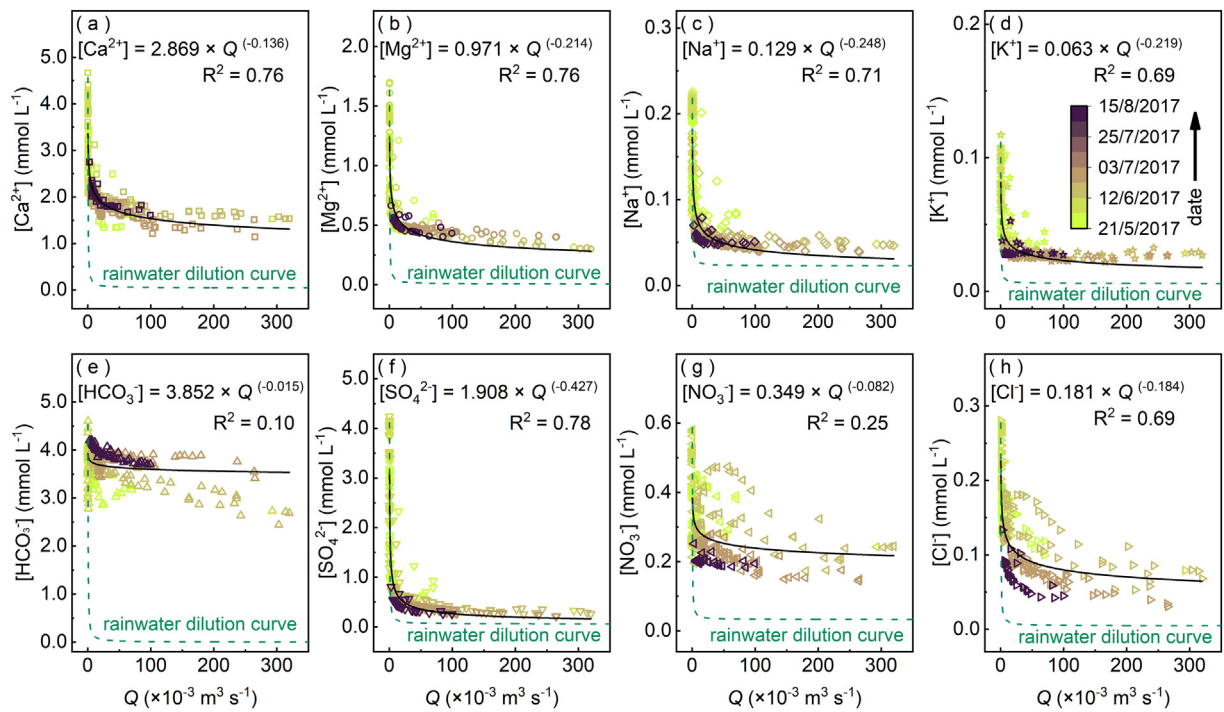


Fig. 4. Power-law relationships ($C = aQ^b$) between concentration (C) of major ions (Ca^{2+} , Mg^{2+} , Na^+ , K^+ , HCO_3^- , SO_4^{2-} , NO_3^- , Cl^-) and discharge (Q). The rainwater dilution curves denote that ions are purely diluted by rainwater at Chenqi catchment.

by dissolved soil CO_2 (Qin et al., 2019), instead of from atmospheric precipitation due to low concentration in rainwater (Zeng et al., 2019). The comparison (Fig. 7(a) and (b)) of high-resolution data (from the wet season in 2017) with seasonal mean values (calculated from monthly samples collected on non-rain days in 2013 (Qin et al., 2019)) suggests that hydrologic flushing during high-flow periods accelerates transportation of carbonate weathering products, partially counteracting the dilution and generating chemostatic behavior. However, the formation of secondary minerals, such as calcite, would consume certain solutes (e.g., Ca^{2+} , Mg^{2+} and HCO_3^-), while the dissolution of exogenous soil CO_2 would supplement HCO_3^- , such that HCO_3^- becomes poorly described by a power-law function and has a stronger chemostatic behavior (Fig. 4(e)) relative to Ca^{2+} and Mg^{2+} . These considerations demonstrate the value of high-resolution data, relative to monthly or seasonal data, for calculating weathering intensity and flux.

The higher b value of $[\text{NO}_3^-]$ (Fig. 4(g)) may be ascribed to the high availability of NO_3^- from anthropogenic sources and underlying biogeochemical processes (e.g., nitrification, eluviation and microbial activities). In this agricultural catchment, NO_3^- mainly derives from reductive nitrogen fertilizer and manure (Yue et al., 2019). Our sampling periods coincide with more intense farming activities. Higher flow during storms can accelerate loss of surficial fertilizers/manure by rapid leaching due to weak buffering capacity in the thin soils in

this karst area (Perrin et al., 2008; Yue et al., 2019). Therefore, $[\text{NO}_3^-]$ shows a stronger flushing response and more variable behavior than most other major ions (Fig. 4). Except for the first event of the wet season when antecedent conditions might be different after a long dry period, $[\text{Cl}^-]$ generally exceeds $[\text{Na}^+]$ and their gap tends to narrow at high discharge (Fig. 7(c)), indicating the additional sources of Cl^- in addition to atmosphere. The response of $[\text{Cl}^-]$ to increasing discharge (Fig. 4(h)) is similar to that of $[\text{NO}_3^-]$ (Fig. 4(g)), and there is a positive correlation between $[\text{NO}_3^-]/[\text{Na}^+]$ and $[\text{Cl}^-]/[\text{Na}^+]$ molar ratios (Fig. 7(d)). This demonstrates that the additional inputs of Cl^- and NO_3^- might come from same sources (e.g., agricultural supply) or be transported by similar processes activated during storm events, but NO_3^- is more available than Cl^- at high discharge.

4.2. Hysteresis analyses for hydrochemistry

A mature karstic system usually contains three types of porosities (Hartmann et al., 2014). The first two, namely micropores (forming during the development of carbonate rock) and small cracks/fissures (appearing during tectonic processes), are normally known as matrix. The third is referred to as conduit, including conduits and big fractures caused by karstification. This structure generates different flow pathways with resulting heterogeneity in water and solute transport

Table 2

Information about eight contrasting storms with different antecedent conditions.

ID	The date and time reaching discharge peak	$Q_{\text{mean-24h}}$ ($\times 10^{-3} \text{ m}^3 \text{ s}^{-1}$)	Time interval (h)	Start discharge ($\times 10^{-3} \text{ m}^3 \text{ s}^{-1}$)	Peak discharge ($\times 10^{-3} \text{ m}^3 \text{ s}^{-1}$)	End discharge ($\times 10^{-3} \text{ m}^3 \text{ s}^{-1}$)	Duration (h)
No. 1	23/5/2017 00:30	0.52	>5 months	0.53	72.05	5.10	3 + 10 = 13
No. 2	12/6/2017 08:15	0.51	474	0.55	331.9	0.42	2 + 56 = 58
No. 3	15/6/2017 10:45	9.11	12	8.06	242.3	4.69	6 + 73 = 79
No. 4	24/6/2017 19:45	18.96	107	16.51	107.1	18.33	7 + 38 = 45
No. 5	27/6/2017 20:15	26.87	2	19.34	179.5	32.00	31 + 32 = 63
No. 6	29/6/2017 17:00	66.60	1	34.07	70.30	41.05	12 + 10 = 22
No. 7	30/6/2017 17:00	54.13	1	40.78	291.4	41.20	13 + 36 = 49
No. 8	13/8/2017 04:00	2.88	104	2.84	99.19	6.63	9 + 48 = 57

Note: $Q_{\text{mean-24h}}$ refers to the mean discharge in the 24 h preceding the storm. Time interval denotes the period from the ending of the last storm to the beginning of this storm according to the storm definition in this study. The equations of storm duration reflect the time taken to reach discharge peak and the time taken to return to initial level.

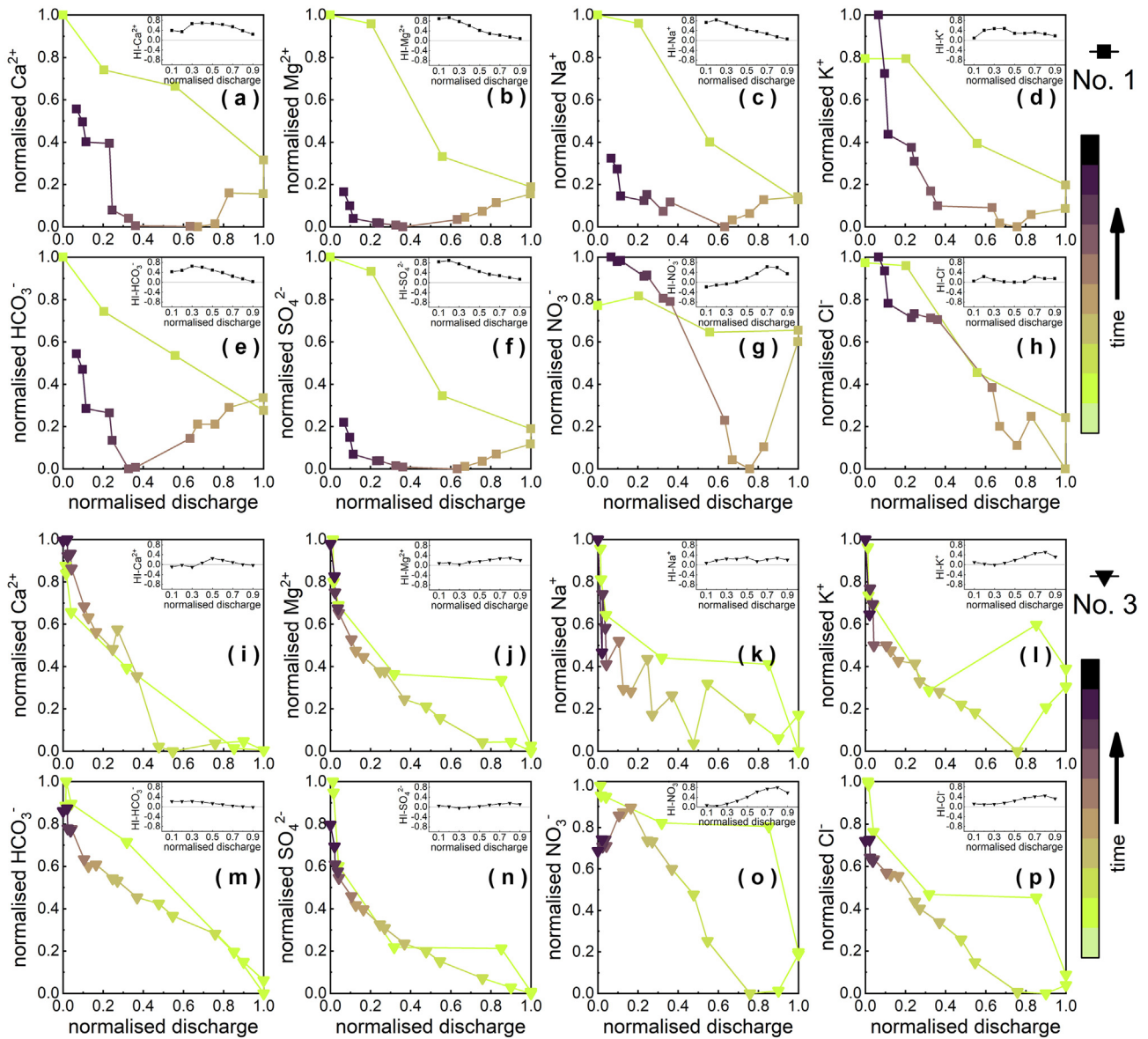


Fig. 5. Plots showing examples for normalised hysteresis loops of ions during storm No. 1 ((a)–(h); the first storm after long dry period) and storm No. 3 ((i)–(p); the storm following No. 2 immediately afterwards). The embedded small graphs exhibit the distribution of HI at each section with 10% increment of the discharge hydrograph during the individual storms.

(Bakalowicz, 2005). Under low-flow conditions, slow diffusion and infiltration through soil or matrix are the dominant recharge patterns, and percolating runoff is largely held in the epikarst aquifer (Williams, 2008). As recharge increases, some stored water percolates downwards to the saturated zone through small fissures, and the remaining flows out quickly in the lower areas through large fractures/conduits as spring water (Trček, 2007).

In this study, the relatively dry period preceding the storm No. 1 lasted over 5 months (Table 2). Under this steadily low-flow condition, there is longer time for water retained in matrix or conduit system to interact with carbonate minerals, producing solutes of higher concentration. When the storm No. 1 occurs after this drier period, the stored water can be flushed out, leading to higher concentration of solutes and lower discharge at the spring outlet at the beginning of the event. The fast transport of ions to the outlet during the rising limb suggests there are potential proximal sources near to, or even within the flow pathways containing large fissures or conduits. However, the ongoing storm can quickly mobilize the sources from pathways, probably by desorption into fluid, or/and by the release from fluid-carbonate interaction along the pathways (Li, 2004). The rapid mobilization and

flushing continuously exhaust these available solutes, so concentrations cannot recover to the initial concentrations as discharge reduces, especially for solutes that are source-limited like SO_4^{2-} . Consequently, instantaneous solute concentrations on the rising limb are much higher than that on the falling limb at the same discharge. Therefore, the first sizable storm after a prolonged dry period normally favors the formation of wide clockwise loops (large HI values) for most solutes. This also provides one explanation why 10%-discharge HI values for ions (excluding NO_3^- and Cl^-) generally exhibit a declining trend with the increasing of normalised discharge (embedded graphs in Fig. 5).

The special type of hysteretic behavior for NO_3^- and Cl^- reflects a mixture of dilution and accretion (Huebsch et al., 2014), that is associated with agricultural characteristics. Fertilized soils can store or accumulate NO_3^- and Cl^- , until rapid flushing of surface soil by storm pulses induces dissolution and entrainment, generating a change in hysteresis response, especially for NO_3^- . HI values of NO_3^- are larger at high discharge than at low discharge during storm No. 1 (Fig. 5(g)), indicating that higher discharge can expand the difference between input and output of NO_3^- , which can partially neutralize the dilution effect but heighten the hysteretic effect. The hysteresis loop of K^+ is slightly

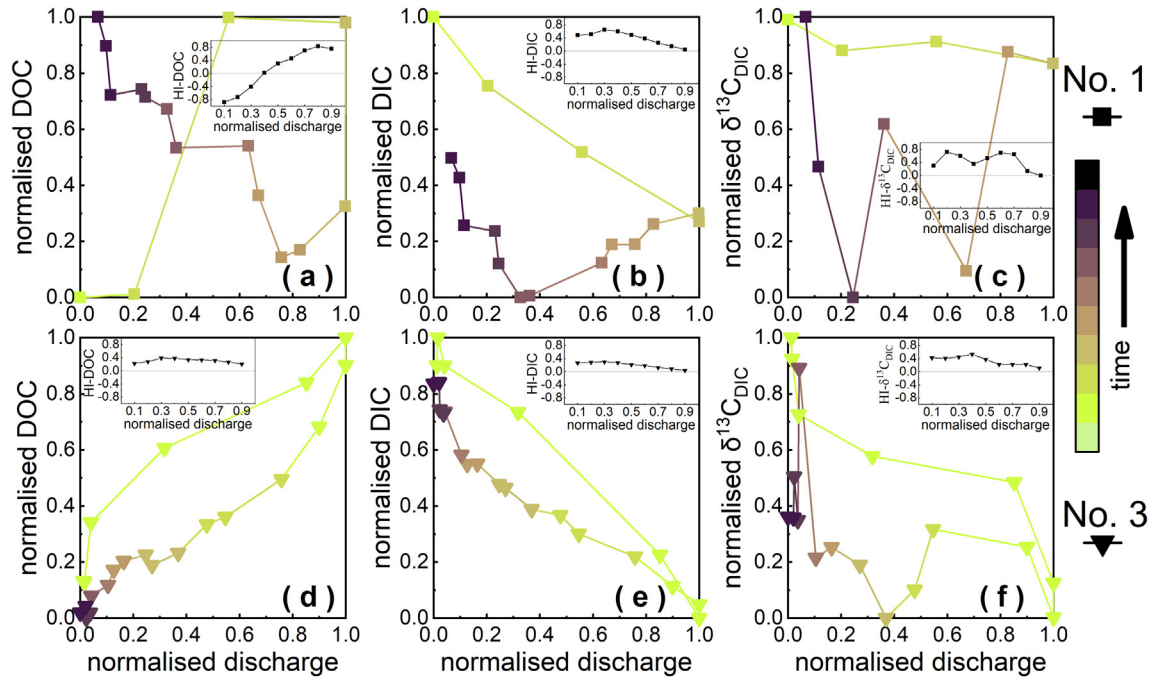


Fig. 6. Plots showing examples for normalised hysteresis loops of DOC, DIC and $\delta^{13}\text{C}_{\text{DIC}}$ during storm No. 1 ((a)–(c); the first storm after long dry period) and storm No. 3 ((d)–(f); the storm following No. 2 immediately afterwards). The embedded small graphs exhibit the distribution of HI at each section with 10% increment of the discharge hydrograph during the individual storms.

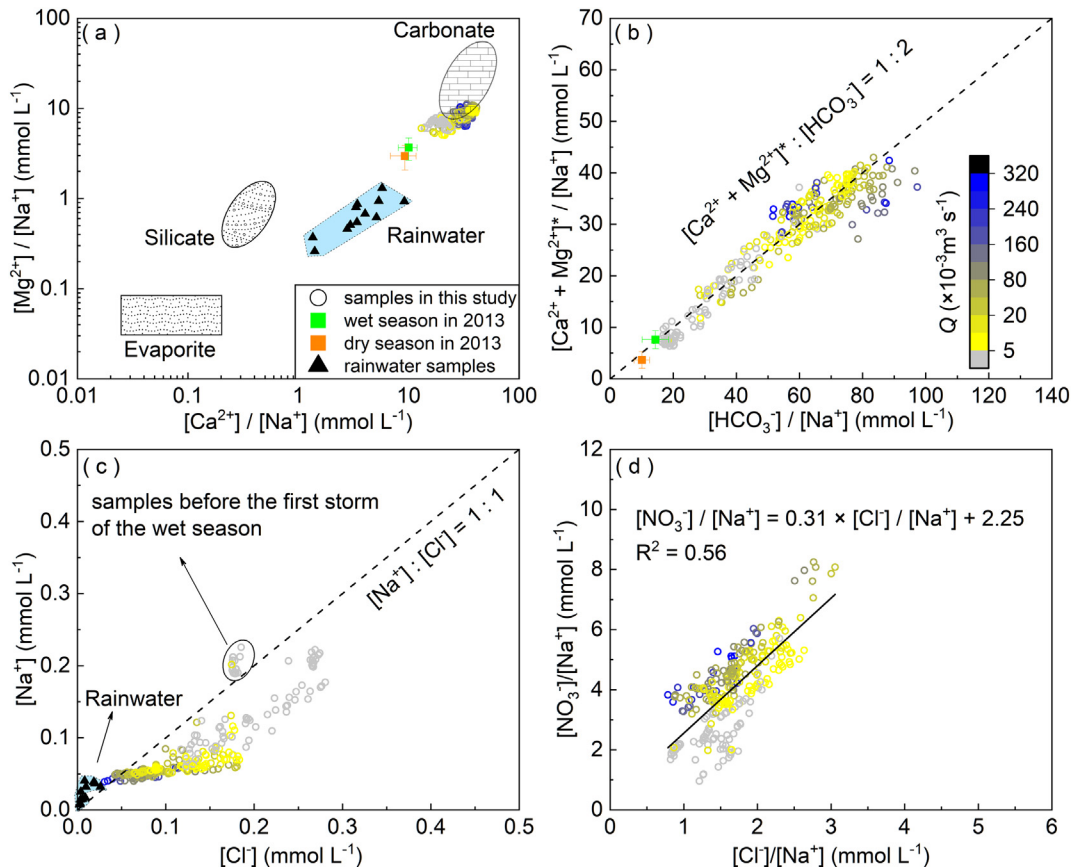


Fig. 7. (a) Relationships between $[\text{Mg}^{2+}]/[\text{Na}^+]$ and $[\text{Ca}^{2+}]/[\text{Na}^+]$ molar ratios. The end-member compositions for carbonates, silicates and evaporites are from Gaillardet et al. (1999). Rainwater data are monthly volume-weighted mean concentrations from October 2016 to September 2017 (unpublished data). Seasonal data in 2013 are calculated from monthly samples which collected on non-rain days at the same sampling point with this study (Qin et al., 2019). (b) Relationships between $[\text{Ca}^{2+} + \text{Mg}^{2+}]^*/[\text{Na}^+]$ and $[\text{HCO}_3^-]/[\text{Na}^+]$ molar ratios, $[\text{Ca}^{2+} + \text{Mg}^{2+}]^* = [\text{Ca}^{2+}] + [\text{Mg}^{2+}] - [\text{SO}_4^{2-}]$. (c) Relationships between $[\text{Na}^+]$ and $[\text{Cl}^-]$. (d) Relationships between $[\text{NO}_3^-]/[\text{Na}^+]$ and $[\text{Cl}^-]/[\text{Na}^+]$ molar ratios.

different at the low discharge segment from fully clockwise trajectories (Fig. 5(d)). This is probably due to enrichment in surface soil resulting from cation exchange and relatively high contents in biomass (Boy et al., 2008), eventually enabling the concentration of K^+ at the end of storm No. 1 to exceed the value at the starting stage.

During storm No. 3, the slimmer hysteresis loops of Ca^{2+} , Mg^{2+} , HCO_3^- , SO_4^{2-} and Na^+ indicate that instantaneous concentrations on the rising limb are similar to those at corresponding discharge on the falling limb. Thus, the hysteresis in storm No. 3 is weaker than No. 1 as there is more dilution and less solute export. This might be caused by any or a combination of the following: (1) more water diluting the same dissolved load; (2) exhaustion of the proximal sources due to flushing during the previous storm (storm No. 2, with 58-hour duration and discharge peak of $331.9 \times 10^{-3} \text{ m}^3 \text{ s}^{-1}$); (3) differences in flow pathway with shorter fluid transit time or/and lesser available storage (Lloyd et al., 2016b; Zhong et al., 2018). Consequently, there is a declining input and an ascending output for solutes, eventually reducing the difference between concentrations on the rising and corresponding falling limb.

A storm with high discharge and long duration can generally transport more substances, especially those with adequate supplementary source areas, such as sediment and phosphorus (Keesstra et al., 2019; Lawler et al., 2006; Lloyd et al., 2016a). In the Chenqi catchment, due to intensive agricultural activities (e.g., fertilization and herding), NO_3^- , Cl^- and K^+ may continue to be available for export during high discharge, rather than being exhausted immediately during a single storm. The discharge peak and duration of storm No. 3 are more triple and six times that of storm No. 1, respectively (Table 2), hence generating higher HI values for these three parameters. After eluviation in the epikarst aquifer, there is exchange of nutrients between the matrix and conduits due to changing water head under different hydrological seasons, but the radial transport from conduits to matrix during high-

flow periods is faster than the release from matrix to conduits during low-flow periods (G.Q. Li et al., 2008; Zhong et al., 2017). This is a conceivable cause for the differences of NO_3^- and Cl^- behaviors among different rain events, resulting in a potential environmental problem that nutrients may affect the quality of karstic groundwater in the agricultural catchment.

Therefore, the behaviors of most weathering products are mostly related to antecedent conditions in addition to karst hydrogeological properties (e.g., thickness, porosity and hydraulic conductivity), and controlled by the process-limited regime. The hysteresis trajectories of K^+ , NO_3^- and Cl^- are also controlled by their availability, storage and transport during individual events in this agricultural catchment.

4.3. Controls on C-Q relationships of dissolved carbon and its dynamic transport

The chemostatic pattern of [DIC] with increasing discharge (Fig. 8 (a)) is similar to that of $[HCO_3^-]$ (Fig. 4(e)) as HCO_3^- dominates DIC species, ranging from 88% to 96% with a mean of 92%. Their chemostatic responses occur: (1) when flow increases and soil CO_2 stored in the matrix porosity is mobilized by fast infiltration (Gaillardet et al., 2018; Pain et al., 2020); (2) undersaturated pCO_2 at high flow allows more soil CO_2 to be transported, which can facilitate carbonate weathering (Jin et al., 2014; Li et al., 2010); (3) the reactive mineral surface area, which is small during low-flow periods as soil moisture is low, will enlarge as discharge increases, facilitating mineral weathering (Clow and Mast, 2010). Nitrification, which is common in the early stage of fertilization (Yue et al., 2015), can accelerate carbonate weathering and soil degradation (Semhi et al., 2000), and so increase DIC export. The change of hysteresis trajectories of DIC between the two storms denotes that either the minimal concentration lags discharge peak, or/and the rate of

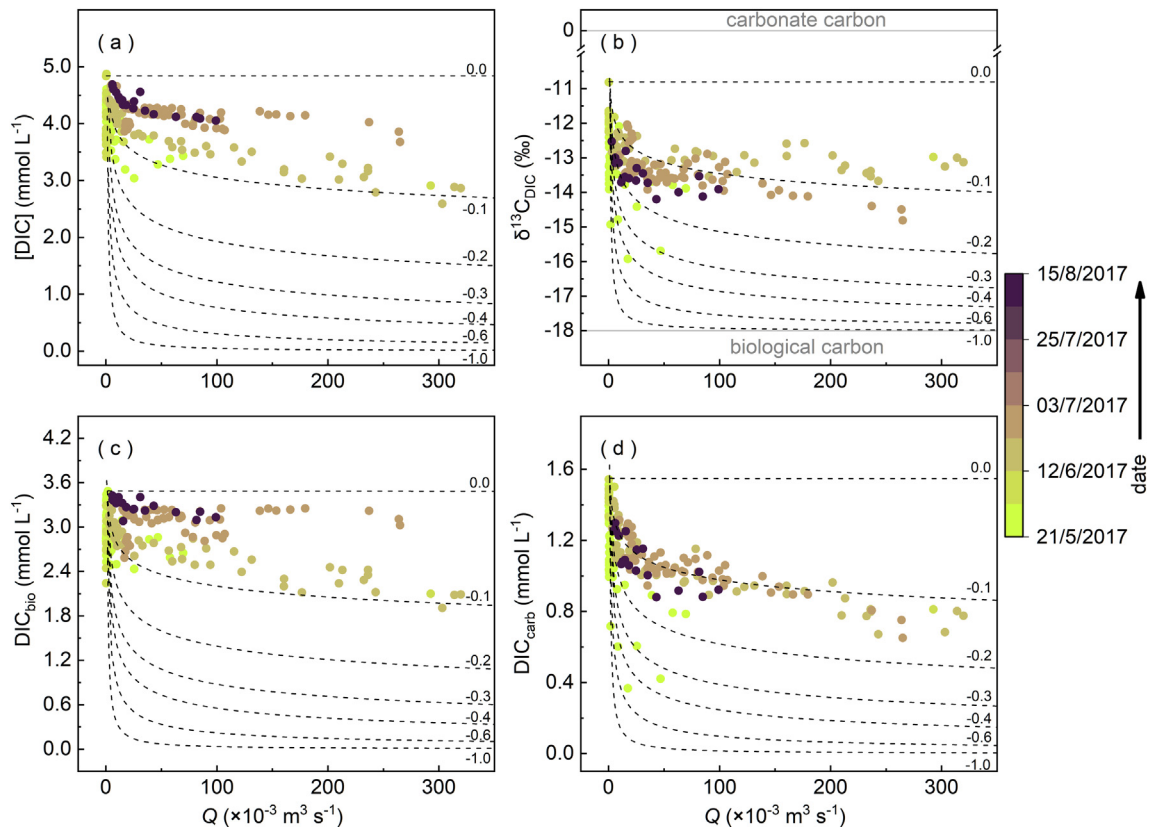


Fig. 8. (a) Relationships between DIC concentrations and discharge. (b) Relationships between $\delta^{13}C_{DIC}$ and discharge. (c) Relationships between DIC_{bio} and discharge. (d) Relationships between DIC_{carb} and discharge. DIC_{bio} and DIC_{carb} refer to the amount of DIC from biological sources and carbonate sources, respectively.

decline in instantaneous concentration on the rising limb surpasses the rate it increases on the falling limb, especially during storm No. 1.

The DWC value of DIC_{bio} is about three times that of DIC_{carb} (2.73 versus 0.92 mmol L^{-1}); both show a chemostatic response (Fig. 8 (c) and (d)), but this is stronger for DIC_{bio} and it is more similar to DIC (Fig. 8(a)). This suggests biological sources should be more important than carbonate sources for DIC dynamic transport under discharge variations. The low concentrations of DOC and few hydrophytes in the spring water mean that DIC_{bio} is most likely from soil than DOC respiration. The high temperature and moisture support biological CO_2 production by respiration and other microbial processes (Li et al., 2010; Liu and Xing, 2012), such as methanogenesis if the system is anoxic, and they can also enhance the rate of primary mineral dissolution (Goudie and Viles, 2012), all of these can increase [DIC]. The chemostatic behavior of DIC_{carb} is mainly controlled by carbonate weathering under different hydrological conditions and biogeochemical processes. The weathering contribution may be reduced when flow velocity increases continually as this activates near-surface flow pathways and shortens time for transportation and deeper fluid-rock interaction (Torres et al., 2015; Zhong et al., 2017). The chemostatic behavior of $\delta^{13}\text{C}_{\text{DIC}}$ (Fig. 8(b)) is the result of mixing from different sources. During the early wet season, $\delta^{13}\text{C}_{\text{DIC}}$ showed a wider range with several lower values. This is mostly because “old” water (dissolving more ^{13}C -depleted biological CO_2) stored in the matrix porosity during the dry period is extruded out and replaced by “new” water during rainfall pulses.

The normalised [DOC] by [Na] increases positively with discharge (Fig. 9(a)), so more DOC is exported by the springs with increasing flowing water. The negative relationship between DOC and DIC (Fig. 9 (b)) demonstrates that there may be transformation of carbon between DIC and DOC, and this could be influenced by changing hydrology. But

compared with [DIC], [DOC] are so low that its changing concentrations with discharge is unlikely to affect $\delta^{13}\text{C}_{\text{DIC}}$ and [DIC].

Both of instantaneous fluxes of DOC (F_{DOC}) and DIC (F_{DIC}) are positively related to discharge but with different exponents b in the fitted power-law function ($F = a \cdot Q^b$), i.e., $b > 1$ and $b < 1$, respectively (Fig. 9(c) and (d)). This difference suggests that transport mechanisms for exogenous influxes of DOC might be different to that of DIC. The hysteretic pattern of DOC indicates that there is a source of DOC mobilized during high-flow periods, most likely from agricultural areas with soil disturbance, such that DOC concentrations increase during the event as observed elsewhere (Mudarra et al., 2011; Xiong et al., 2018). The different hysteresis behaviors of DOC between the two storms likely reflect the change of dominant flow (Bowes et al., 2005), from slow baseflow (through small fissures/matrix) during storm No. 1 to quick flow (through large fractures/conduits) during storm No. 3 as the epikarst becomes wetter. The transport-limited regime seems to be more important for DOC transport than antecedent conditions.

The mixing of multiple sources with different $\delta^{13}\text{C}$ and processes that fractionate $\delta^{13}\text{C}$ jointly render the hysteresis response of $\delta^{13}\text{C}_{\text{DIC}}$ complex. Storm pulses can increase reactive mineral surface areas and further expedite carbonate dissolution (Clow and Mast, 2010), generating ^{13}C -enriched DIC. However, rapid flow can reduce time available for fluid-rock interaction (Tipper et al., 2006) and transport soil CO_2 , both of which drive $\delta^{13}\text{C}_{\text{DIC}}$ to be more ^{13}C -depleted. Additionally, other factors such as turbulent flow (McClanahan et al., 2016), molecular diffusion of CO_2 (Amiotte-Suchet et al., 1999), and the degradation of organic compounds (Ogrinc et al., 2005), can also cause isotopic fractionation of the DIC pool or introduce a new source and so alter bulk $\delta^{13}\text{C}_{\text{DIC}}$. Nevertheless, the angular trajectories of $\delta^{13}\text{C}_{\text{DIC}}$ for the two case storms display some hysteresis and indicate that in this K-CZ, high-flow conditions

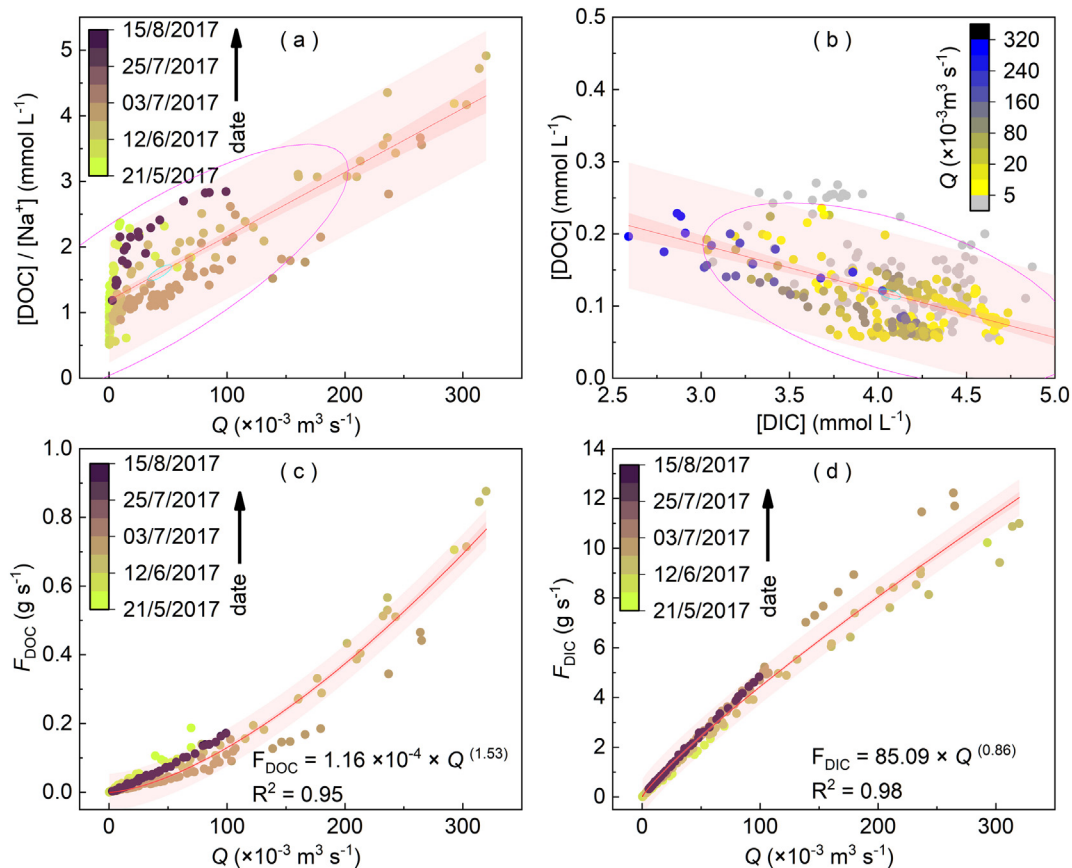


Fig. 9. (a) The relationship between discharge and [DOC]/[Na⁺] molar ratios. (b) The relationship between DIC and DOC concentrations. (c) Relationships between flux of DOC (F_{DOC}) and discharge. (d) Relationships between flux of DIC (F_{DIC}) and discharge. The little cyan circle and big carmine circle refer to confidence ellipse of mean and prediction, respectively. (For interpretation of the references to color in this figure legend, the reader is referred to the web version of this article.)

can generally cause ^{13}C -depletion. Thus, DIC dynamics and $\delta^{13}\text{C}_{\text{DIC}}$ are possibly controlled by a process-limited regime associated with biological processes and hydrological conditions in the karstic critical zone.

5. Conclusions

Through using high-frequency monitoring at a spring outlet in a karstic critical zone (K-CZ), this research comprehensively considers the chemostatic and hysteretic response of hydrochemistry and dissolved carbon to discharge variations. In this K-CZ observatory in Southwestern China, all parameters displayed chemostatic responses with different intensities to discharge variations. The chemostatic behavior of Na^+ , K^+ and SO_4^{2-} were weaker and mainly controlled by rainwater dilution. Both NO_3^- and Cl^- were affected by flushing as discharge increased and showed a more heterogeneous response. Dissolved soil CO_2 transported by through-flow enhanced carbonate weathering, enabling HCO_3^- , Ca^{2+} and Mg^{2+} to maintain chemostatic response to the increasing discharge. Biologically-derived DIC demonstrated a stronger chemostatic behavior and was the most important driving force for DIC behavior under discharge variations. Supplementary DOC was exported by increasing discharge, but in still too low concentration to significantly affect $\delta^{13}\text{C}_{\text{DIC}}$ and DIC concentration. The hysteresis analysis revealed the response of parameters to individual rainstorms. The clockwise hysteretic loops of most ions (excluding NO_3^- and Cl^-) indicated their fast transit from proximal source areas to the sampling point. The hysteretic behaviors of NO_3^- and Cl^- were different and influenced by a mixture of dilution and flushing from agricultural soils. The change of hysteretic behaviors of NO_3^- , Cl^- and DOC in different events represented differences in availability, storage and transport during storms, which was influenced by transport-limited regime and related to storm intensity/magnitude in the critical zone. The hysteresis behaviors of weathering products and DIC were controlled by a process-limited regime which was strongly associated with the timing of storms and antecedent conditions. In addition, the hydrogeological properties, including thickness, porosity and hydraulic conductivity, can also affect elemental hysteresis behaviors. Additional in-depth analyses are needed in the future to reveal water-carbon coupling mechanisms in order to model carbon dynamics in the karstic critical zone.

Declaration of competing interest

The authors declare that they have no known competing financial interests or personal relationships that could have appeared to influence the work reported in this paper.

Acknowledgements

This study was jointly funded by the National Natural Science Foundation of China [grant numbers 41571130072, 41861144026], the National Key Research and Development Program of China [grant number 2016YFA0601002]; and the UK Natural Environment Research Council [grant number NE/N002806/1]. The authors thank Sen Xu and Jie Zeng for their help in the sample collections. The authors would also thank the anonymous reviewers for their useful comments and the editor for guidance.

References

- Amiotte-Suchet, P., Aubert, D., Probst, J.L., Gauthier-Lafaye, F., Probst, A., Andreux, F., Viville, D., 1999. $\delta^{13}\text{C}$ pattern of dissolved inorganic carbon in a small granitic catchment: the Strengbach case study (Vosges mountains, France). *Chem. Geol.* 159 (1), 129–145.
- Amiotte-Suchet, P., Probst, J.-L., Ludwig, W., 2003. World-wide distribution of continental rock lithology: implications for the atmospheric/soil CO_2 uptake by continental weathering and alkalinity river transport to the oceans. *Glob. Biogeochem. Cycles* 17 (2), 1038 (7/1–7/13).
- Bakalowicz, M., 2005. Karst groundwater: a challenge for new resources. *Hydrogeol. J.* 13 (1), 148–160.
- Baker, E.B., Showers, W.J., 2019. Hysteresis analysis of nitrate dynamics in the Neuse River, NC. *Sci. Total Environ.* 652, 889–899.
- Beaulieu, E., Godd eris, Y., Donnadi e, Y., Labat, D., Roelandt, C., 2012. High sensitivity of the continental-weathering carbon dioxide sink to future climate change. *Nat. Clim. Chang.* 2 (5), 346–349.
- Bowes, M.J., House, W.A., Hodgkinson, R.A., Leach, D.V., 2005. Phosphorus-discharge hysteresis during storm events along a river catchment: the River Swale, UK. *Water Res.* 39 (5), 751–762.
- Bowes, M.J., Jarvie, H.P., Halliday, S.J., Skeffington, R.A., Wade, A.J., Loewenthal, M., Gozzard, E., Newman, J.R., Palmer-Felgate, E.J., 2015. Characterising phosphorus and nitrate inputs to a rural river using high-frequency concentration-flow relationships. *Sci. Total Environ.* 511, 608–620.
- Boy, J., Valarezo, C., Wilcke, W., 2008. Water flow paths in soil control element exports in an Andean tropical montane forest. *Eur. J. Soil Sci.* 59 (6), 1209–1227.
- Brantley, S., White, T.S., White, A.F., Sparks, D., Richter, D., Pregelzer, K., Derry, L., Chorover, J., Chadwick, O., April, R., Anderson, S., Amundson, R., 2006. Frontiers in Exploration of the Critical Zone: Report of a Workshop Sponsored by the National Science Foundation (NSF), October 24–26, 2005 (Newark, DE, 30 pp).
- Buckerfield, S.J., Quilliam, R.S., Waldron, S., Naylor, L.A., Li, S., Oliver, D.M., 2019. Rainfall-driven *E. coli* transfer to the stream-conduit network observed through increasing spatial scales in mixed land-use paddy farming karst terrain. *Water Res.* X 5, 100038.
- Chen, X., Zhang, Z., Soulsby, C., Cheng, Q., Binley, A., Jiang, R., Tao, M., 2018. Characterizing the heterogeneity of karst critical zone and its hydrological function: an integrated approach. *Hydrol. Process.* 32 (19), 2932–2946.
- Clark, I.D., Fritz, P., 1997. *Environmental Isotopes in Hydrogeology*. Lewis Publishers, New York.
- Clow, D.W., Mast, M.A., 2010. Mechanisms for chemostatic behavior in catchments: implications for CO_2 consumption by mineral weathering. *Chem. Geol.* 269 (1–2), 40–51.
- Council, N.R., 2001. *Basic Research Opportunities in Earth Science*. The National Academies Press, Washington, DC (168 pp).
- Darwiche-Criado, N., Com n, F.A., Sorando, R., S nchez-P rez, J.M., 2015. Seasonal variability of NO_3^- mobilization during flood events in a Mediterranean catchment: the influence of intensive agricultural irrigation. *Agric. Ecosyst. Environ.* 200, 208–218.
- de Montety, V., Martin, J.B., Cohen, M.J., Foster, C., Kurz, M.J., 2011. Influence of diel biogeochemical cycles on carbonate equilibrium in a karst river. *Chem. Geol.* 283, 31–43.
- Dianwu, Z., Seip, H.M., 1991. Assessing effects of acid deposition in Southwestern China using the magic model. *Water Air Soil Pollut.* 60 (1), 83–97.
- Ding, H., Liu, C.-Q., Zhao, Z.-Q., Li, S.-L., Lang, Y.-C., Li, X.-D., Hu, J., Liu, B.-J., 2017. Geochemistry of the dissolved loads of the Liao River basin in northeast China under anthropogenic pressure: chemical weathering and controlling factors. *J. Asian Earth Sci.* 138, 657–671.
- Dreybrodt, W., 1988. *Processes in Karst Systems*. Springer, Heidelberg Germany.
- Ferrant, S., Laplanche, C., Durbe, G., Probst, A., Dugast, P., Durand, P., Sanchez-Perez, J.M., Probst, J.L., 2013. Continuous measurement of nitrate concentration in a highly event-responsive agricultural catchment in south-west of France: is the gain of information useful? *Hydrol. Process.* 27 (12), 1751–1763.
- Gaillardet, J., Allegre, C.J., Dupre, B., Louvat, P., 1999. Global silicate weathering and CO_2 consumption rates deduced from the chemistry of large rivers. *Chem. Geol.* 159, 3–30.
- Gaillardet, J., Calmels, D., Romero-Mujalli, G., Zakharova, E., Hartmann, J., 2018. Global climate control on carbonate weathering intensity. *Chem. Geol.* 527. <https://doi.org/10.1016/j.chemgeo.2018.05.009>.
- Godsey, S.E., Kirchner, J.W., Clow, D.W., 2009. Concentration-discharge relationships reflect chemostatic characteristics of US catchments. *Hydrol. Process.* 23 (13), 1844–1864.
- Goudie, A.S., Viles, H.A., 2012. Weathering and the global carbon cycle: geomorphological perspectives. *Earth-Sci. Rev.* 113 (1–2), 59–71.
- Hartmann, A., Goldscheider, N., Wagener, T., Lange, J., Weiler, M., 2014. Karst water resources in a changing world: review of hydrological modeling approaches. *Rev. Geophys.* 52 (3), 218–242.
- Huang, X., Fang, N.F., Zhu, T.X., Wang, L., Shi, Z.H., Hua, L., 2018. Hydrological response of a large-scale mountainous watershed to rainstorm spatial patterns and reforestation in subtropical China. *Sci. Total Environ.* 645, 1083–1093.
- Huebsch, M., Fenton, O., Horan, B., Hennessy, D., Richards, K.G., Jordan, P., Goldscheider, N., Butscher, C., Blum, P., 2014. Mobilisation or dilution? Nitrate response of karst springs to high rainfall events. *Hydrol. Earth Syst. Sci.* 18 (11), 4423–4435.
- Jin, J., Zimmerman, A.R., Moore, P.J., Martin, J.B., 2014. Organic and inorganic carbon dynamics in a karst aquifer: Santa Fe River Sink-Rise system, north Florida, USA. *J. Geophys. Res. Biogeosci.* 119 (3), 340–357.
- Keesstra, S.D., Davis, J., Masselink, R.H., Casali, J., Peeters, E.T.H.M., Dijkstra, R., 2019. Coupling hysteresis analysis with sediment and hydrological connectivity in three agricultural catchments in Navarre, Spain. *J. Soils Sediments* 19 (3), 1598–1612.
- Khadka, M.B., Martin, J.B., Jin, J., 2014. Transport of dissolved carbon and CO_2 degassing from a river system in a mixed silicate and carbonate catchment. *J. Hydrol.* 513, 391–402.
- Lawler, D.M., Petts, G.E., Foster, I.D., Harper, S., 2006. Turbidity dynamics during spring storm events in an urban headwater river system: the Upper Tame, West Midlands, UK. *Sci. Total Environ.* 360 (1–3), 109–126.
- Li, G., 2004. *Laboratory Simulation of Solute Transport and Retention in a Karst Aquifer*. Florida State University (PhD Dissertation).
- Li, S., Bush, R.T., 2015. Changing fluxes of carbon and other solutes from the Mekong River. *Sci. Rep.* 5, 16005.
- Li, G.Q., Loper, D.E., Kung, R., 2008a. Contaminant sequestration in karstic aquifers: experiments and quantification. *Water Resour. Res.* 44 (2), W02429. <https://doi.org/10.1029/2006WR005797>.

- Li, S.-L., Calmels, D., Han, G., Gaillardet, J., Liu, C.-Q., 2008b. Sulfuric acid as an agent of carbonate weathering constrained by $\delta^{13}\text{C}_{\text{DIC}}$: examples from Southwest China. *Earth Planet. Sci. Lett.* 270 (3–4), 189–199.
- Li, S.-L., Liu, C.-Q., Li, J., Lang, Y.-C., Ding, H., Li, L., 2010. Geochemistry of dissolved inorganic carbon and carbonate weathering in a small typical karstic catchment of Southwest China: isotopic and chemical constraints. *Chem. Geol.* 277 (3–4), 301–309.
- Liu, W., Xing, M., 2012. Isotopic indicators of carbon and nitrogen cycles in river catchments during soil erosion in the arid Loess Plateau of China. *Chem. Geol.* 296–297, 66–72.
- Lloyd, C.E., Freer, J.E., Johnes, P.J., Collins, A.L., 2016a. Using hysteresis analysis of high-resolution water quality monitoring data, including uncertainty, to infer controls on nutrient and sediment transfer in catchments. *Sci. Total Environ.* 543 (2016), 388–404.
- Lloyd, C.E.M., Freer, J.E., Johnes, P.J., Collins, A.L., 2016b. Technical note: testing an improved index for analysing storm discharge-concentration hysteresis. *Hydrol. Earth Syst. Sci.* 20 (2), 625–632.
- Martin, J.B., 2017. Carbonate minerals in the global carbon cycle. *Chem. Geol.* 449, 58–72.
- McClanahan, K., Polk, J., Groves, C., Osterhoudt, L., Grubbs, S., 2016. Dissolved inorganic carbon sourcing using $\delta^{13}\text{C}_{\text{DIC}}$ from a karst influenced river system. *Earth Surf. Process. Landf.* 41 (3), 392–405.
- Meybeck, M., Vörösmarty, C., 1999. Global transfer of carbon rivers. *Glob. Change News.* 37, 18–19.
- Mudarra, M., Andreo, B., Baker, A., 2011. Characterisation of dissolved organic matter in karst spring waters using intrinsic fluorescence: relationship with infiltration processes. *Sci. Total Environ.* 409 (18), 3448–3462.
- Musolf, A., Schmidt, C., Selle, B., Fleckenstein, J.H., 2015. Catchment controls on solute export. *Adv. Water Resour.* 86, 133–146.
- Ogrinc, N., Fontolan, G., Faganeli, J., Covelli, S., 2005. Carbon and nitrogen isotope compositions of organic matter in coastal marine sediments (the Gulf of Trieste, N Adriatic Sea): indicators of sources and preservation. *Mar. Chem.* 95 (3–4), 163–181.
- Pain, A.J., Martin, J.B., Young, C.R., Valle-Levinson, A., Mariño-Tapia, I., 2020. Carbon and phosphorus processing in a carbonate karst aquifer and delivery to the coastal ocean. *Geochim. Cosmochim. Acta* 269, 484–495.
- Perrin, A.-S., Probst, A., Probst, J.-L., 2008. Impact of nitrogenous fertilizers on carbonate dissolution in small agricultural catchments: implications for weathering CO_2 uptake at regional and global scales. *Geochim. Cosmochim. Acta* 72 (13), 3105–3123.
- Qin, C., Li, S.L., Yue, F.J., Xu, S., Ding, H., 2019. Spatiotemporal variations of dissolved inorganic carbon and controlling factors in a small karstic catchment, Southwestern China. *Earth Surf. Process. Landf.* 44 (12), 2423–2436.
- Rode, M., Wade, A.J., Cohen, M.J., Hensley, R.T., Bowes, M.J., Kirchner, J.W., Arhonditsis, G.B., Jordan, P., Kronvang, B., Halliday, S.J., Skeffington, R.A., Rozemeijer, J.C., Aubert, A.H., Rinke, K., Jomaa, S., 2016. Sensors in the stream: the high-frequency wave of the present. *Environ. Sci. Technol.* 50 (19), 10297–10307.
- Semhi, K., Suchet, P., Clauer, N., Probst, J.-L., 2000. Impact of nitrogen fertilizers on the natural weathering-erosion processes and fluvial transport in the Garonne basin. *Appl. Geochem.* 15 (6), 865–878.
- Tipper, E.T., Bickle, M.J., Galy, A., West, A.J., Pomies, C., Chapman, H.J., 2006. The short term climatic sensitivity of carbonate and silicate weathering fluxes: insight from seasonal variations in river chemistry. *Geochim. Cosmochim. Acta* 70 (11), 2737–2754.
- Torres, M.A., West, A.J., Clark, K.E., 2015. Geomorphic regime modulates hydrologic control of chemical weathering in the Andes–Amazon. *Geochim. Cosmochim. Acta* 166, 105–128.
- Trček, B., 2007. How can the epikarst zone influence the karst aquifer hydraulic behaviour? *Environ. Geol.* 51 (5), 761–765.
- van Geer, F.C., Kronvang, B., Broers, H.P., 2016. High-resolution monitoring of nutrients in groundwater and surface waters: process understanding, quantification of loads and concentrations, and management applications. *Hydrol. Earth Syst. Sci.* 20 (9), 3619–3629.
- Voss, B.M., Peucker-Ehrenbrink, B., Eglinton, T.I., Fiske, G., Wang, Z.A., Hoering, K.A., Montluçon, D.B., LeCroy, C., Pal, S., Marsh, S., Gillies, S.L., Janmaat, A., Bennett, M., Downey, B., Fanslau, J., Fraser, H., Macklam-Harron, G., Martinec, M., Wiebe, B., 2014. Tracing river chemistry in space and time: dissolved inorganic constituents of the Fraser River, Canada. *Geochim. Cosmochim. Acta* 124, 283–308.
- Waldron, S., Marian Scott, E., Vihermaa, L.E., Newton, J., 2014. Quantifying precision and accuracy of measurements of dissolved inorganic carbon stable isotopic composition using continuous-flow isotope-ratio mass spectrometry. *Rapid Commun. Mass Spectrom.* 28 (10), 1117–1126.
- Williams, G.P., 1989. Sediment concentration versus water discharge during single hydrologic events in rivers. *J. Hydrol.* 111 (1), 89–106.
- Williams, P.W., 2008. The role of the epikarst in karst and cave hydrogeology: a review. *Int. J. Speleol.* 37 (1), 1–10.
- Xiong, B., Zhang, J., Peng, T., Hao, Z., Gao, Y., 2018. Concentration variations and flux estimation of dissolved carbon in karst spring of a typical karst area. *Environ. Sci.* 39 (11), 4991–4998 (in Chinese).
- Yuan, D., Cai, G., 1988. *The Science of Karst Environment*. Chongqing Publishers, Chongqing China (1–332 pp, in Chinese).
- Yue, F.-J., Li, S.-L., Liu, C.-Q., Lang, Y.-C., Ding, H., 2015. Sources and transport of nitrate constrained by the isotopic technique in a karst catchment: an example from Southwest China. *Hydrol. Process.* 29 (8), 1883–1893.
- Yue, F.-J., Waldron, S., Li, S.-L., Wang, Z.-J., Zeng, J., Xu, S., Zhang, Z.-C., Oliver, D.M., 2019. Land use interacts with changes in catchment hydrology to generate chronic nitrate pollution in karst waters and strong seasonality in excess nitrate export. *Sci. Total Environ.* 696, 134062.
- Zeng, J., Yue, F.-J., Wang, Z.-J., Wu, Q., Qin, C.Q., Li, S.-L., 2019. Quantifying depression trapping effect on rainwater chemical composition during the rainy season in karst agricultural area, southwestern China. *Atmos. Environ.* 218, 116998.
- Zhang, L., Song, X., Xia, J., Yuan, R., Zhang, Y., Liu, X., Han, D., 2011. Major element chemistry of the Huai River basin, China. *Appl. Geochem.* 26 (3), 293–300.
- Zhang, Z., Chen, X., Soulsby, C., 2017. Catchment-scale conceptual modelling of water and solute transport in the dual flow system of the karst critical zone. *Hydrol. Process.* 31 (19), 3421–3436.
- Zhang, Z., Chen, X., Cheng, Q., Soulsby, C., 2019. Storage dynamics, hydrological connectivity and flux ages in a karst catchment: conceptual modelling using stable isotopes. *Hydrol. Earth Syst. Sci.* 23 (1), 51–71.
- Zhong, J., Li, S.L., Tao, F., Yue, F., Liu, C.Q., 2017. Sensitivity of chemical weathering and dissolved carbon dynamics to hydrological conditions in a typical karst river. *Sci. Rep.* 7, 42944.
- Zhong, J., Li, S.L., Liu, J., Ding, H., Sun, X.L., Xu, S., Wang, T.J., Ellam, R.M., Liu, C.Q., 2018. Climate variability controls on CO_2 consumption fluxes and carbon dynamics for monsoonal rivers: evidence from Xijiang river, Southwest China. *J. Geophys. Res. Biogeosci.* 123 (8), 2553–2567.